# A data-driven wind-to-current response function and application to Ocean surface current estimates

Clément Ubelmann[1], J. Thomas Farrar[2], Bertrand Chapron[3], Lucile Gaultier[4], Laura Gomez-Navarro[5], Marie-Héléne Rio[5], and Gérald Dibarboure[7]

[1]Datlas, France
[2]Woods Hole Oceanographic Institution, MA, USA
[3]Ifremer, France
[4]Ocean Data Lab, France
[5]Utrecht University, The Netherlands
[5]Esa-Esrin, Italy
[7]CNES, France

**Correspondence:** Clément Ubelmann (clement.ubelmann@datlas.fr)

**Abstract.** This study investigates ~~modeling the~~ the reconstruction of wind-driven ~~current using observed wind stress and an empirically estimated~~ currents based on an empirical impulse response function~~for the wind-driven current response to wind forcing. Convolution of the data-driven impulse response function with the wind forcing gives an estimate of the wind-driven part of the current . We estimate this data-driven convolution operator using~~ . Surface current observations derived from drifting buoy data and wind-stress from the ERA5 ~~reanalysis winds and observations of surface currents from drifting buoys. The response of the currents to wind forcing~~ reanalyses are used to derive the response function. The function is expected to depend on the ocean mixed-layer depth and more generally the turbulent viscosity profile with spatio-temporal variations, but we only consider seasonally-modulated and spatial variations~~in the training~~. Despite this crude approximation, the simplified response function ~~explains~~ can explain a significant portion of the current variability ~~. Indeed, when the function is applied to the ERA5 wind-stress, the surface current estimate compares reasonably well with independent observations (not used in the training)~~in independent observations from other times and location.

A practical application is the release of a new total surface current ~~estimates such as the Globcurrent CMEMS MOB-TAC product (denoted WOC in the study). Compared to existing products~~ based on the same ~~datasets, but here containing also the unsteady part of the wind driven currents (the inertial currents). The~~ input datasets, such as the CMEMS MOB-TAC (Guinehut (2021)) surface current product, the WOC estimates are designed to include higher frequency content, in particular in the inertial band. Beyond successful validation, the characteristics of the response function (amplitudes and phases) reveal interesting properties of the upper-ocean variability. The function shows some similarities to one derived theoretically from a simple 1-layer (slab) model, but also differences that highlight the value of fitting the function to the data without the use of an explicit dynamical model. This opens perspectives for studying some dependencies between subsurface variables and the response function, particularly interesting in the context of future spaceborne Doppler scatterometers such as ODYSEA (Rodríguez et al. (2019)), expected to provide simultaneous wind and current observations: this instrument could indirectly probe subsurface properties through the synoptically-observed response function.

## 1 Introduction

The transfer of momentum and energy across the air-sea interface provides sources of oceanic ~~motions. Resulting~~ motion. The resulting upper ocean surface currents can then cover a wide range of temporal and spatial scales. A major component, called the geostrophic current, equilibrates the pressure gradient force and the Coriolis force. ~~Pressure-gradients~~ Pressure gradients are currently well observed by satellite altimetry at spatial and temporal scales down to about 150km wavelength and 20-day periods (Ballarotta et al., 2019). Another important component, called ~~the~~ wind-driven current, is more directly related to atmospheric wind stress forcing. ~~Over a range of depths not small compared to a ratio of the water velocity to the local Coriolis frequency, Coriolis effects become important. Direction and magnitude of the mean velocity field then vary with depth. A net transport in the upper ocean takes place, the Ekman transport, oscillatory in time with the inertial frequency, relative to and superimposed on the geostrophic motion.~~ This includes both Ekman currents, which result from a balance of the "frictional" force (the wind stress at the surface and subsurface turbulent momentum flux) and the Coriolis force, and inertial currents, which result from the resonant response of the upper ocean to changing winds. Wind-driven currents can reach large amplitudes, often exceeding the geostrophic current. ~~Wind-driven currents~~ They are of interest for many scientific applications (e.g. Shrira and Almelah, 2020) and play an important role in the ~~the ocean's energy budget~~ energy budget of the ocean (Flexas et al., 2019), but also for practical and societal applications, such as surface drift and accumulation of marine litter (Higgins et al., 2020; Cunningham et al., 2022). Besides seldom satellite synthetic aperture radar estimates (Chapron et al., 2005), total surface currents are not ~~not~~ directly observed at synoptic scale by satellite observations. However, estimates can be obtained from ~~the knowledge of~~ knowledge of the surface wind stress. In this study, we investigate the use of a data-driven response function ~~.~~ relating the wind-stress and the ageostrophic surface current to empirically capture some part of the wind-driven currents. ~~Despite the simplicity of the response function that excludes interactions with other components, it leads to an inverse linear problem, to further easily exploit the global drifter database to learn an effective ocean response to the wind forcing.~~

~~Some recent and extensive~~ Some recent studies have been dedicated to the theoretical aspects of the response of upper-ocean currents to wind forcing. In particular, ~~Elipot and Gille (2009); Lilly and Elipot (2021)~~ Elipot and Gille (2009) and Lilly and Elipot (2021) focused on the spectral transfer function between wind-stress and current, with extensive ~~analysis~~ analyses of its dependencies ~~with viscosity profiles in the ocean subsurface layers~~on viscosity profiles as a function of depth. We focus here on the closely related impulse response function, or just response function, that relates the ocean response to the wind forcing in the physical space. The impulse response function ~~follows~~ is the Fourier transform of the spectral transfer function (Bendat and Piersol, 2010, p. 29, 26-27). ~~Such a~~ The construction of the response function from real data and its applications to estimate the surface current at synoptic scales have not been fully explored yet. ~~Some operational~~ Existing operational surface current products include an estimation of ~~the Ekman component~~ ageostrophic current related to wind forcing, such as the [OSCAR] or the [CMEMS-MOB-TAC)] datasets also based on a response function ~~(?)[now operational in CMEMS, or the OSCAR dataset]. However, their response function~~ as described in (Rio et al., 2014). Their response function from wind-stress to surface current is a single complex-scalar function therefore limited to low-frequency estimates~~.~~, designed to empirically capture Ekman currents.

To generalize the approach and, in particular, to better resolve the inertial frequency band, here we examine the empirical fit of a full response function acting across a broader spectral range. As detailed in Lilly and Elipot (2021), the local response of the ocean to wind forcing at different frequencies can be described with a complex ~~Fourier-space transfer function, equivalent to complex time-convolution~~ frequency response function, which is equivalent to use of a complex impulse response function in physical space.

In this study, we ~~apply the convolution response-function concept to real observations and show the benefits of estimating it empirically~~therefore propose to explore the empirical fit of a convolution response function and show its ability to reconstruct some ageostrophic surface current directly related to wind forcing. This is made possible ~~because of~~ thanks to the growing number of accumulated drifter data at high time-frequency (hourly outputs). The first practical application is the estimation of ~~the~~ some wind-driven surface current ~~at all times~~ directly from the wind-stress reanalyses available. Also, a more exploratory objective is to analyze whether the empirical response function constructed from the data alone can help us obtain new insights into ocean physics (like vertical mixing) and subsurface ocean properties (like mixed-layer depth). This is strongly motivated by the prospect of future spaceborne Doppler missions such as ODYSEA (Rodríguez et al. (2019)) designed to observe simultaneously the surface wind and current at synoptic scale. Indeed, if the sparse drifter database can only provide spatio-temporally averaged response functions at best, the space-borne observation may allow a monitoring of the response function to probe subsurface characteristics.

~~The study is performed globally (70°S to 80°N). The time extension covers 2010-2020, a long period necessary to reach convergence in the response function estimate. Section~~ The manuscript is organized as follows : section 2 presents all the datasets ~~. Section~~ used in this study, as input or validation datasets. Then, section 3 ~~presents the motivation behind the determination of the~~ focuses on the methodology behind the response function. Section 4 covers the application to surface current estimates, including the validation, and section 5 explores some characteristics of the response function and its characteristics with respect to subsurface dynamics. Finally, section 6 concludes and discusses some perspectives.

## 2 Datasets~~: ERA5 wind stress, surface drifter velocities and altimeter-derived geostrophic current~~

~~Three datasetsare considered in this study~~The empirical fit, performed globally over 70°S to 80°N, is based on three input datasets: the surface drifter velocities (sparse total current observations), the geostrophic ~~current and the Ocean surface wind-stress,~~ velocities (to estimate the ageostrophic current by difference with the total current), and the wind stress from the ERA5 reanalysis, all covering the period from years 2010 to 2020. An additional dataset of total surface current, based on similar input datasets but using a different algorithm, is considered for comparison to our total surface current estimates.

The surface drifter velocities have been extracted from the ~~global drifter~~ [Global-Drifter-Program] database (Elipot et al. (2016)) in its version 2.0.1. Only the 'drogued' drifters are considered in the main experiment, representative of the current at 15m depth which is the focus of this study. ~~The velocity variables (pre-processed from the positions)~~ The velocities at hourly frequency are used ~~. Both Argo~~ (estimated jointly from the unevenly distributed observed positions). Both ARGOS and GPS data are ~~used~~ considered to allow the 10-year extension of the study with a maximum number of data, although the GPS data, collected with a different technology, are more accurate (Yu et al. (2019)) and fairly dominant after 2015.

The geostrophic ~~velocity dataset from CMEMS (Taburet et al. (2019)),~~ velocities used in this study were derived from muti-satellite altimetry maps ~~, have been~~ (Taburet et al. (2019)). The data, already processed in velocity units (m/s), were extracted from the [CMEMS-MOB-TAC] dataset. We co-located the data at all drifters hourly positions. A linear interpolation scheme ~~is~~ was used between the daily 1/4° spatial grid and the ~~drifters. These estimates are used to substract from the total velocity measured by~~ drifter positions. By difference with the total current from the drifters, ~~in order to isolate~~ we have an estimation of the ageostrophic component representative of the ~~$u$~~ $u_e$ variable in the equations presented next section~~.~~, at all drifter positions.

The ~~ERA5~~ surface wind-stress ~~product at hourly resolution~~ data were extracted from the [ERA5] product provided by the Copernicus Marine service at hourly mean and output frequency on a 0.25° spatial grid (Hersbach et al. (2020))~~is used as the forcing term described~~. We also co-located the data at all drifters hourly position, including the 8-day history in order to integrate the $\tau_0$ variable in the equations presented next section.

For validation purposes, the total surface current from the CMEMS-MOB-TAC dataset have also been used and co-located at the drifter positions.

Finally, our WOC output dataset (the acronym stands for the ESA "World Ocean Circulation" project) presented in the following, arising from the first three datasets, can be accessed here: [WOC]. The data ~~were provided by the Copernicus service.~~ have been written on the same grid as the total surface current from CMEMS-MOB-TAC to facilitate comparisons. Note that both the total surface current from CMEMS MOB-TAC and WOC have the same geostrophic component.

Figure 1 illustrates the ~~main~~ input and comparison datasets, during an event where a strong atmospheric front resolved by ERA5 ~~triggers~~ seems to trigger inertial currents captured by a drifter. On the upper-right panel, the drifter features clear oscillations after ~~the passage of the~~ crossing the atmospheric front. The oscillations are very clear both on the drifter trajectory and on the derived zonal current shown on the bottom panel. Although the oscillations may combine several effects possibly including tidal signals, we think they are mostly inertial signal that could be reconstructed from the wind forcing. This gives some confidence on the reliability of the datasets to explore the ~~unsteady-Ekman response.~~ wind-driven current response. The geostrophic current shown in green explains a large part of the low-frequency motion not directly related to wind-forcing. The CMEMS MOB-TAC total surface current that will be our baseline for comparison, shown in blue, seems to capture some accurate ageostrophic current (beyond the geostrophic one) but not the oscillatory part.

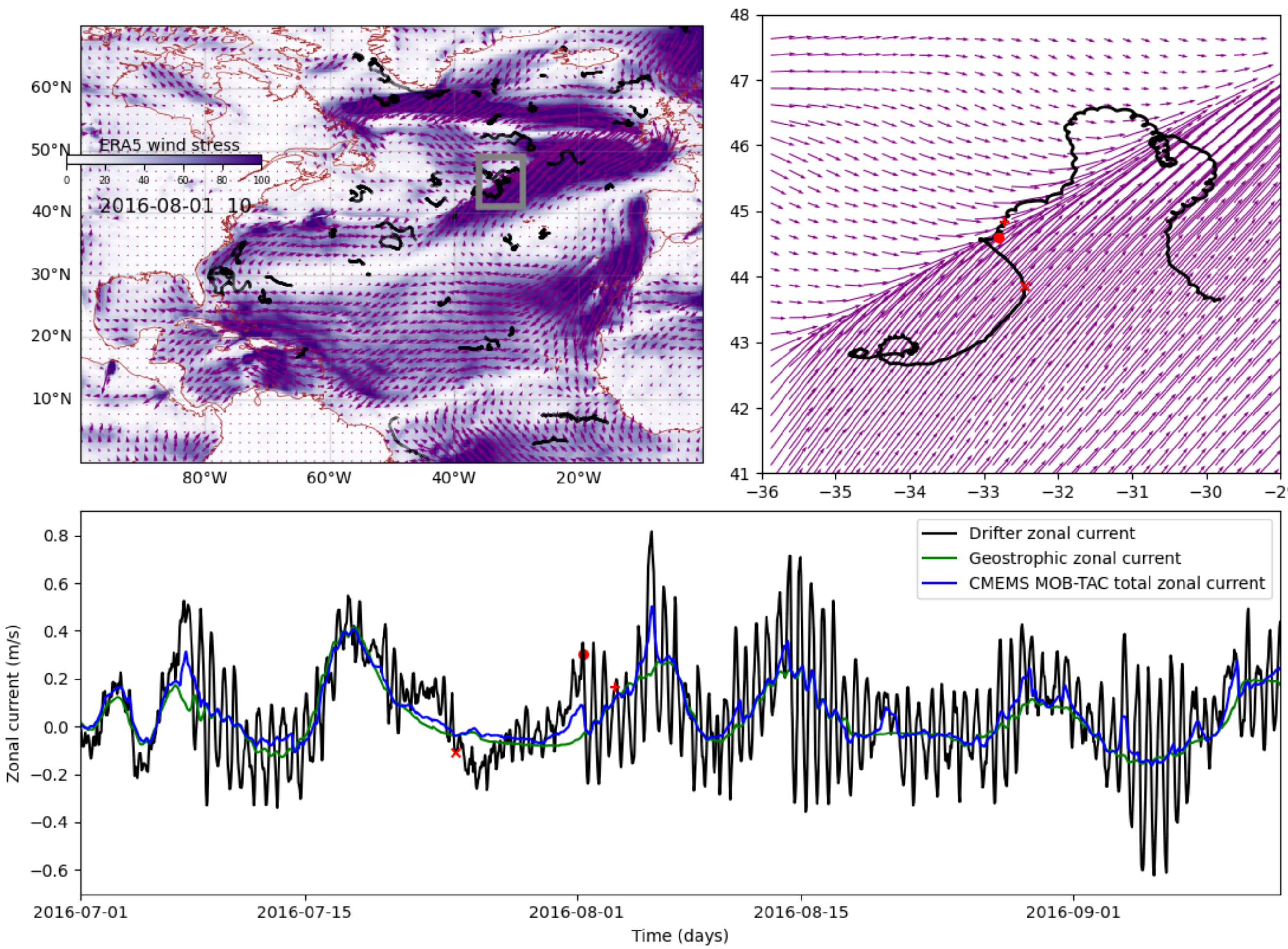


**Figure 1.** Illustration of the main datasets used in the study. Upper-left panel : a snapshot of the ERA5 wind stress superimposed with the ensemble of drifter positions over +/- 20 days. Upper right: zoom of the first panel highlighting the presence of a drifter near a strong atmospheric front (the red dot is the position at the ~~present time~~ time of the wind-stress map, the red "x" and "+" 8 days before and 2 days after respectively). Lower panel: time series of the zonal velocities derived from the drifter trajectory (black), with a colocation of the geostrophy ~~from altimetry~~ (green) ~~with added CMEMS Ekman estimate~~ and the total surface zonal current from CMEMS-MOB-TAC (blue). ~~showing that inertial oscillations are triggered after the crossing of the atmospheric front.~~

## 3 The data-driven response function

### 3.1 The rationale for a response function

The equations governing the horizontal currents in the upper ocean can be written approximately as (e.g., Gill, 1982, p. 320), (neglecting horizontal advection) as (e.g., Gill, 1982, p. 320):

$$\frac{\partial u}{\partial t}\frac{\partial u_x}{\partial t} - fv fu_y = \frac{1}{\rho}\left(-\frac{\partial p}{\partial x} + \frac{\partial \tau^x}{\partial z}\frac{\partial \tau_x}{\partial z}\right) \tag{1}$$

$$\frac{\partial v}{\partial t}\frac{\partial u_y}{\partial t} + fu_x = \frac{1}{\rho}\left(-\frac{\partial p}{\partial y} + \frac{\partial \tau^y}{\partial z}\frac{\partial \tau_y}{\partial z}\right) \tag{2}$$

where $\mathbf{u} = (u, v)$ $(u_x, u_y)$ is the horizontal current vector, $f$ is the local Coriolis parameter (or inertial frequency)signed Coriolis parameter, $\rho$ is the density, $p$ is the pressure and $\boldsymbol{\tau} = (\tau^x, \tau^y)$ $(\tau_x, \tau_y)$ is the horizontal stress vector. (Horizontal advection terms have been neglected. ) All variables except $f$ are depth dependent. Assuming there is no nonlinear dependence of $\boldsymbol{\tau}$ $(\tau_x, \tau_y)$ or $p$ on $\mathbf{u}$, $(u_x, u_y)$ these equations are linear. Some simple parameterizations of the momentum fluxes $(\tau_x, \tau_y)$ in terms of the velocity are linear (e.g., constant eddy viscosity, linear drag), but more complicated ones are not (e.g., mixing schemes that involve a critical Richardson number). In reality, we expect a nonlinear relationship between $(\tau_x, \tau_y)$ and $(u_x, u_y)$, as well influence of other factors (e.g., surface heat fluxes), but we will assume a linear relationship as a starting point here.

We are interested in how the upper ocean responds to wind forcing. We can conceptually separate the velocity vector $\mathbf{u}_{total}$ $(u_x, u_y)$ into a pressure-driven component $\mathbf{u}_g$ and a stress-driven component (or unsteady-Ekman component) $\mathbf{u}_e$ $(u_{e_x}, u_{e_y})$, which is governed by:

$$\frac{\partial u_e}{\partial t}\frac{\partial u_{e_x}}{\partial t} - fv_e fu_{e_y} = \frac{1}{\rho}\frac{\partial \tau^x}{\partial z}\frac{\partial \tau_x}{\partial z} \tag{3}$$

$$\frac{\partial v_e}{\partial t}\frac{\partial u_{e_y}}{\partial t} + fu_{e e_x} = \frac{1}{\rho}\frac{\partial \tau^y}{\partial z}\frac{\partial \tau_y}{\partial z} \tag{4}$$

It is convenient to to express the vectors $\mathbf{u_e} = (u_{e_x}, u_{e_y})$ and $\boldsymbol{\tau} = (\tau_x, \tau_y)$ using complex notation as $\mathbf{u_e} = u_{e_x} + iu_{e_y}$ and $\boldsymbol{\tau} = \tau_x + i\tau_y$ (where $i = \sqrt{-1}$). Then Eqns. 3-4 can be written in a single equation:

$$\frac{\partial \mathbf{u_e}}{\partial t} + if\mathbf{u_e} = \frac{1}{\rho}\frac{\partial \boldsymbol{\tau}}{\partial z} \tag{5}$$

To relate the wind-driven current, $\mathbf{u}_e$, to the wind-stress forcing (or the value of $\boldsymbol{\tau}$)

The impulse response function provides an important way of characterizing a constant-parameter linear system and relating its inputs to its outputs. For any arbitrary input forcing at the surface, $\boldsymbol{\tau}_0$, an impulse response formulation writes $\boldsymbol{\tau_0}(t)$, the output of the system, $\boldsymbol{u_e}(z,t)$ at depth $z$ can be written,

$$\mathbf{u}_e \boldsymbol{u_e}(xz, y, t) = \int_{-T}^{0} G_0^T \boldsymbol{G_z}(t')\, \boldsymbol{\tau}_0 \boldsymbol{\tau_0}(t + t\, t - t')\, dt' \tag{6}$$

where $G$ $\boldsymbol{G_z}$, the impulse response function of the system at depth $z$, is a complex function of time lag $t'$, and the integral from $-T$ to 0 0 to $T$ (positive time only) expresses the fact that the output $\boldsymbol{u_e}$ can only depend on the time-history of the wind stress forcing . We assume the unsteady-Ekman current past forcing $\boldsymbol{\tau}\,(t-t'<t)$. If we assume that the wind-driven current is only affected by this the wind history over a limited time , and (before momentum fluxes dissipate the upper layer energy), we might choose $T$ is set to be about a week. to be on the order of a few days. As discussed in the next section, $T = 8$ days will be a reasonable value.

The inversion problem is to retrieve $G$, given drifter observations of $\mathbf{u}_e$ (approximated by the velocity derived from the position minus the geostrophic current from altimetry, as illustrated on the bottom panel of Figure 2), and from the Eulerian history of ERA5 wind stress at each drifter location (upper panel of Figure 2). These two series, here shown for 75 days for a specific drifter, are generated using all drifters (except for a few , withheld for validation) in the studt area over the 10 years. Example of Lagrangian time series of the ERA5 wind stress (zonal and meridional components) co-located at a drifter position (upper panel) and time series of the drifter-derived ageostrophic velocity (lower panel).

Note, additional signals are obviously present, combining imperfect geostrophy estimates, ageostrophic motions not resolved by altimetry, errors from the drifter measurements, etc... We assume these additional signals are uncorrelated with the wind-driven motions we aim to retrieve.

Vertically integrating Eqns 3-4 To get some intuition for what kinds of physics might be captured by an empirically estimated impulse response function, it is helpful to consider a simplified model. Vertically integrating Eqn 5 from the surface to some depth $H$, the vertically averaged velocity $(\bar{u}_e, \bar{v}_e)$ are: $\bar{\boldsymbol{u}}_{\boldsymbol{e}}$ is expressed as:

$$\frac{\partial \bar{u}_e}{\partial t} - f_e = \frac{\tau_0^x - \tau_H^x}{\rho H}\frac{\partial \bar{v}_e}{\partial t}\frac{\partial \bar{\boldsymbol{u}}_{\boldsymbol{e}}}{\partial t} + f_e i f \bar{\boldsymbol{u}}_{\boldsymbol{e}} = \frac{\tau_0^y - \tau_H^y}{\rho H}\frac{\boldsymbol{\tau_0} - \boldsymbol{\tau_H}}{\rho H} \tag{7}$$

where $(\tau_H^x, \tau_H^y)$ correspond to turbulent stress $\boldsymbol{\tau}_H$ is the value of the turbulent stress vector at depth $H$. These equations are This equation is one version of the "slab model" , that is commonly used to model mixed-layer inertial currents (e.g., Plueddemann and Farrar, 2006; Alford, 2020). Considering $(\tau_H^x, \tau_H^y)$, If we parameterize the stress at depth $H$ as being linearly proportional to the layer-averaged velocity, $(\tau_H^x, \tau_H^y) = r\rho H(\bar{u}_e, \bar{v}_e)$, so that $\boldsymbol{\tau_H} = r\rho H \bar{\boldsymbol{u}}_{\boldsymbol{e}}$, where $r$ is a scalar damping coefficient, we obtain the well-known "damped slab" model of the mixed layer is recovered (e.g., D'Asaro, 1985): (e.g., D'Asaro, 1985):

$$\frac{\partial \bar{u}_e}{\partial t} - f_e = \frac{\tau_0^x}{\rho H} - r_e \frac{\partial \bar{v}_e}{\partial t}\frac{\partial \bar{\mathbf{u}}_{\mathbf{e}}}{\partial t} + f_e (r + if)\bar{\boldsymbol{u}}_{\boldsymbol{e}} = \frac{\tau_0^y}{\rho H} - r_e \frac{\boldsymbol{\tau_0}}{\rho H} \tag{8}$$

Writing the vector components in complex notation ($Z \equiv \bar{u}_e + i\bar{v}_e$ and $T \equiv \bar{\tau}_0^x + i\bar{\tau}_0^y$), the damped slab model is given by

We can derive the spectral transfer function by taking the Fourier transform of Eq. 8 (with $\bar{\boldsymbol{U}}_{\boldsymbol{e}}(\omega)$ and $\boldsymbol{T_0}(\omega)$ indicating the Fourier transforms of $\bar{\boldsymbol{u}}_{\boldsymbol{e}}(t)$ and $\boldsymbol{\tau_0}(t)$):

$$\frac{\partial Z}{\partial t} + \bar{\boldsymbol{U}}_{\boldsymbol{e}}(r + if\omega)Z = \frac{T}{H}\frac{1}{\rho H(r + i(\omega + f))}\boldsymbol{T_0}(\omega) \tag{9}$$

which has the impulse response function in the physical space:

$$G\boldsymbol{G_0}(t) = \frac{e^{-rt}}{H}\frac{e^{-rt}}{\rho H}e^{-ift}. \tag{10}$$

$G(t)$ $\boldsymbol{G_0}(t)$ is defined for $t = 0$ to $t = \infty$. For the damped slab model, the impulse response function oscillates at frequency $f$ with an amplitude that is inversely proportional to mixed-layer depth, $H$, and decays with time with an e-folding decay timescale of $1/r$. One can "run" the damped slab model convolving $G(t)$ with an observed wind stress $T\ (\bar{\tau}_0^x + i\bar{\tau}_0^y)$. This example of $\boldsymbol{G}$ function will serve as a baseline for comparison with the empirical $\boldsymbol{G}$ fitted from the data in this study, and possible departures from it may reveal various kinds of additional physics that cannot be described by a single damping parameter.

One *could* simply fit the parameters in Eqns **??** or 10 to the data to make a model of

### 3.2 Resolution of the inverse problem to fit G

The inversion problem consists of finding the $\boldsymbol{G_z}$ function at depth $z = 15$m (noted $\boldsymbol{G}$ in the following) from drifter observations $\boldsymbol{u_{obs}}$, the inertial response. As noted by Plueddemann and Farrar (2006), Alford (2020), and others, co-located geostrophic current $\boldsymbol{u_{g_{obs}}}$ and the surface stress $\boldsymbol{\tau_0}$ such as:

$$\boldsymbol{u_{obs}} - \boldsymbol{u_{g_{obs}}} = \int_0^T \boldsymbol{G}(t')\boldsymbol{\tau_0}(t-t')dt' + \boldsymbol{\epsilon} \tag{11}$$

$(\boldsymbol{u_{obs}} - \boldsymbol{u_{g_{obs}}})$, noted $\boldsymbol{u_{e_{obs}}}$ in the following, represents our best observed estimate of ageostrophic current, that is supposed to contain the linear response to wind forcing $\boldsymbol{\tau_0}(t)$ plus additional signal represented by $\boldsymbol{\epsilon}$. $\boldsymbol{\epsilon}$ may contain some missing geostrophy (errors in $\boldsymbol{u_{g_{obs}}}$), errors in the drifter measurement of current, the result of error integration in the knowledge of $\boldsymbol{\tau_0}(t)$ and any ageostrophic current that would not be captured by the convolution of $\boldsymbol{G}$ with the forcing $\boldsymbol{\tau_0}(t)$. Note that $\boldsymbol{\epsilon}$ is not necessarily small, but this should not prevent to find a meaningful $\boldsymbol{G}$ function if a large amount of observations are processed.

As an illustration, Figure 2 shows some time series of the forcing $\boldsymbol{\tau_0}(t)$ (upper panel) and the damping of mixed-layer inertial motions involves various kinds of physics (e.g., turbulent momentum transport, wave radiation stresses) acting on different timescales, and so a single damping parameter cannot adequately represent all of the processes removing momentum and energy from the near-surface ocean. Thus, it is preferable to estimate $G$ in Eqn 6 without having to rely on the approximations beyond those in Eqns 3-4. ageostrophic observed current $\boldsymbol{u_{e_{obs}}}$ (lower panel). Solving the Eq. 11 consists in finding the convolution operator transforming the upper panel series into the lower panel series, both written under the complex mathematical form (Real part for the zonal direction and Imaginary part for the meridional direction). Here only 75 days of data is shown for one specific drifter, but the whole series over 2010-2020 are considered.

### 3.3 The degrees of freedom for G

Finding $\boldsymbol{G}$ that minimizes $\boldsymbol{\epsilon}$ in Eq. 11 is a linear inverse problem that can be solved by minimizing the following cost function :

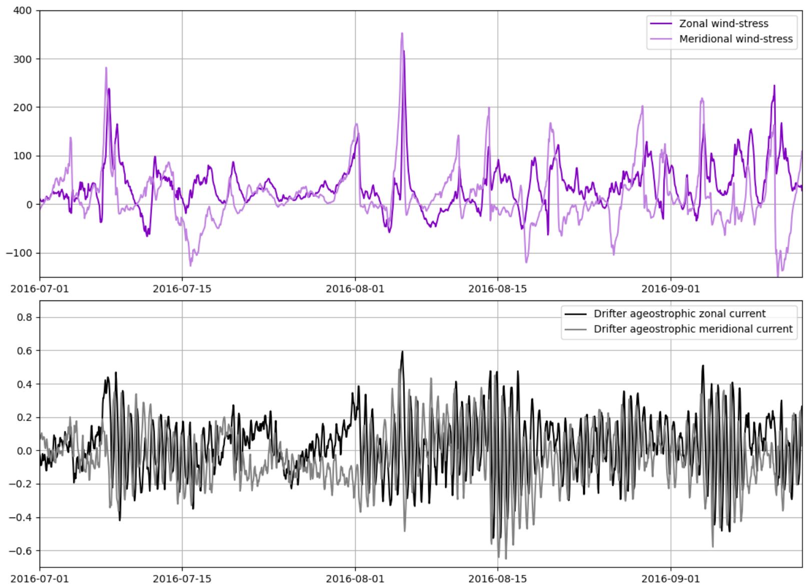


**Figure 2.** Example of Lagrangian time series of the ERA5 wind stress (zonal and meridional components) co-located at a drifter position (upper panel) and time series of the drifter ageostrophic velocity (lower panel).

$$J = \| \int_0^T \boldsymbol{G}(t')\boldsymbol{\tau_0}(t-t')dt' - \boldsymbol{u_{e_{obs}}} \|^2 \tag{12}$$

Over the oceans, very different conditions of stratification (and mixed layer depth in particular) can be found , so we cannot expect the $G$ $\boldsymbol{G}$ response function to be uniform. Nevertheless, the amount of drifter data is limited and to avoid over-fitting issues, we cannot let G $\boldsymbol{G}$ vary totally freely. In order to have a good compromise, we defined a reduced space where a $G$ the $\boldsymbol{G}$ function can vary with latitude , and seasonally. If $\eta$ and seasons, which seemed to be the dominant variables. The impact of these assumptions on potential weaknesses of the method will be discussed in conclusions. In practice, we choose 1° latitudinal steps and a single harmonic at 1-year period to fit in time. If $\boldsymbol{\eta}$ is a parameter vector in this reduced space, $G$ $\boldsymbol{G}$ is decomposed by a series of linear operators under the form:

$$\mathbf{G(x,y,t,t') = \Gamma(t')S(t)L(x,y)}\eta \boldsymbol{G}(y,t,t') = \boldsymbol{\Gamma}(t')\boldsymbol{S}(t)\boldsymbol{L}(y)\boldsymbol{\eta} \tag{13}$$

where L $\boldsymbol{L}$ is a bi-linear spatial interpolator transforming the ensemble of values for $\eta$ $\boldsymbol{\eta}$ in the parameter space into a local set of parameters at location $(x,y)$latitude $y$. Then, the operator $S(t)$ applies the seasonality reducing into a subset of parameters at the time of the year $\boldsymbol{S}(t)$ applies the the 1-year harmonic (in practice, one constant, one sine and one cosine functions are defined at the annual-frequency). Finally, $\Gamma$ $\boldsymbol{\Gamma}$ converts the subset of parameters into the response function value at relative time $t'$. $\boldsymbol{G}(t')$. The number of parameters to fit is directly proportional to the time extension over which $\boldsymbol{G}$ is defined. Some sensitivity tests have been conducted to find an optimal time extension, based on the maximum of explained variance over independent drifter data. Globally, the optimal was around 8 days, which is certainly a compromise between the actual extension of $\boldsymbol{G}$ (the wind-driven linear response time) and possible overfitting due to the limited amount of drifter data. Note that this optimal value may actually vary with latitudes, but we did not implement this capability.

### 3.3 Resolution of the inverse problem to fit G

The series of operators transforming $\eta$ $\boldsymbol{\eta}$ into the local (spatially and seasonally) convolution function are linear. The convolution operator is also linear. Therefore, the wind-driven current vector $u_e$ at the difter observations at the drifter location can be written as :

$$\mathbf{u_e} = \mathbf{M}\eta + \epsilon$$

where $\mathbf{M}$ is a $\boldsymbol{u_{e_{obs}}} = \boldsymbol{M\eta} + \boldsymbol{\epsilon}$ where $\boldsymbol{M}$ is the linear operator including the successive construction of $G$ and the convolution $\boldsymbol{G}$ and the integration operation with the wind-stress, all linear with respect to $\eta$ . This inverse problem can be solved by minimizing the following cost function :

$\boldsymbol{\eta}$ . The cost function of Eq. 12 becomes:

$$J = \|\boldsymbol{M\eta} - \boldsymbol{u_{obs}}\|^2 \tag{14}$$

We used that can be easily solved with a conjugate gradient descent involving iterative computations of the gradient of the cost function:

$$\nabla J = \frac{1}{2}\boldsymbol{M^T}(\boldsymbol{M\eta} - \boldsymbol{u_{obs}}) \tag{15}$$

In practice, the adjoint operator $\mathbf{M^T}$ $\boldsymbol{M^T}$ is applied from the adjoint of the linear operations in Eq. 13 and from the adjoint of the convolution Eq. 6. For the problem considered, the convergence was reached after about a hundred iterations.

## 4 Application to surface current estimates and validation

A direct application of the response function fitted from the drifters is an estimation of the linear response part of the wind-driven current over a continuous time/space grid as it is for the input ERA5 wind-stress from the reanalysis(our WOC estimate). This was performed over the 10-year of study on the 0.25° resolution grid of the ERA5 input datadataset. The upper panels of figure 3 show snapshots of the current obtained with the response function (right, called the WOC estimates hereafter) WOC current compared with the current form the CMEMS Ekman model from the CMEMS MOB-TAC (left). On the right, higher amplitudes are reached, with an imprint of oscillatory patterns after the passage crossing of the atmospheric front near 45°N, 40°E. The lower panel shows these estimations as a function of time in red and blue respectively (with added geostrophy represented in green) co-located with a drifter in black (this drifter was excluded from the training).

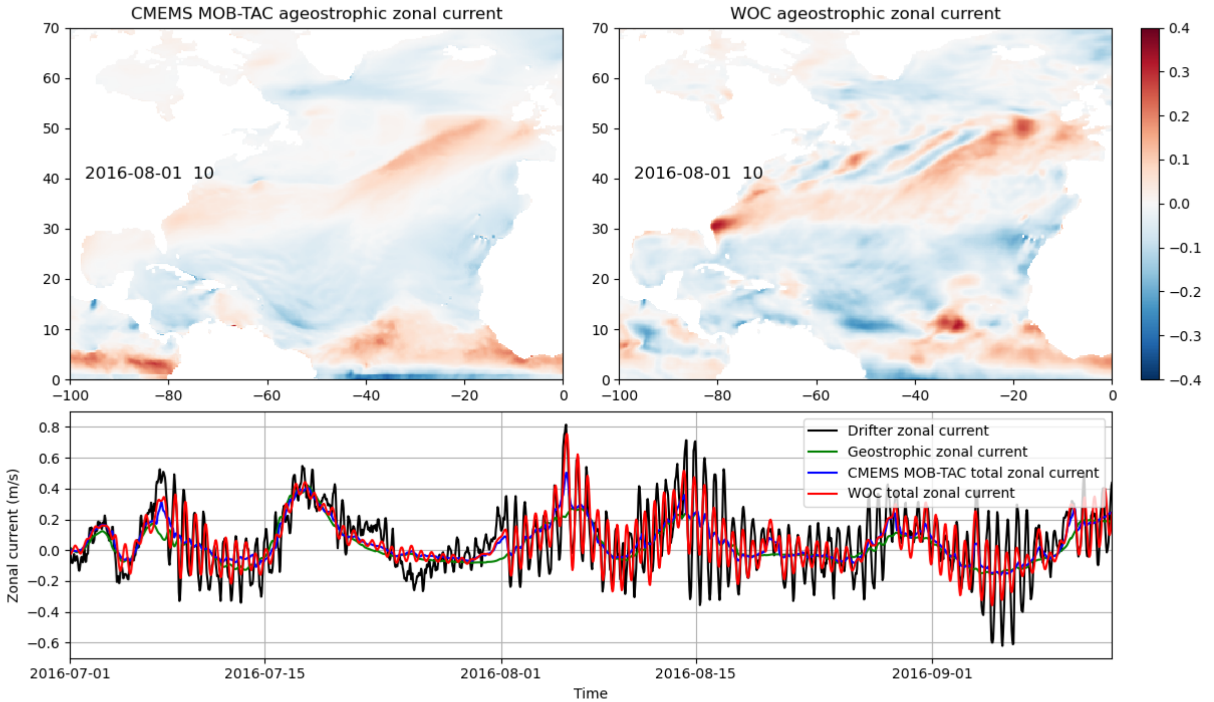


**Figure 3.** Illustrations of the wind-driven Snapshots of the ageostrophic zonal current from the CMEMS MOB-TAC (upper left) and from the WOC response-function approach (upper right). Bottom : time series from the response-function approcah (red line) colocated at in independant drifter position, after addition of an estimate of the Geostrophic zonal current (green line). The estimated current captures many of the details of the zonal current observed independently by the drifter (black line).of the total zonal current measured by an independent drifter (black), with a co-location of the geostrophic, CMEMS MOB-TAC total and WOC total zonal current in green, blue and red respectively

A significant part of the observed inertial oscillations are ageostrophic current is captured by the WOC response function estimation. In particular, some near-inertial oscillations seems to be reconstructed with a phase that seems quite accurate in this example (we picked a case with particularly intense inertial oscillation signal for the illustration). Not surprisingly, the amplitude is attenuated since the estimation is designed to minimize root mean square, and there is a significant part of unresolved signal. The latter may be explained by two main sources: the imperfect wind and the locally specific subsurface turbulent viscosity conditions not captured by the climatological variations of G (mixed layer or more generally the density profile). Additional sources may also be the results of interaction between the wind-driven current and the mesoscales (e.g. Young and Jelloul (1997)) or simply the presence of submesoscale currents. The amplitude is overall attenuated with respect to observations certainly because of the unresolved processes mentioned in the previous section.

Some quantitative diagnostics can be applied to the ensemble of independent drifters to assess the reconstruction skills more quantitatively and in all situations (not only during strong wind events). On the top panel panels of figure 4, we represent in black the power time-frequency spectrum of the observed drifter current between 1000 hours and 2 hours (in the clockwise direction on the left panel and counter-clockwise on the right panel) averaged over the oceans between 40°N and 50°N. The thick colored lines represent the resolved energy by the different estimations: geostrophic in green, ~~Globcurrent/CMEMS (including Ekman) estimation~~ total current from CMEMS MOB-TAC in blue, and the WOC estimation ~~of wind-driven current including the inertial component,~~ in red. As anticipated by the resolved oscillations on Figure 3, the red spectrum features a clear peak at the inertial frequency (near 18 hours at these latitudes in the clockwise panel corresponding to anticyclonic motion), of about 40% of the energy seen by the drifters (black). We note that the sub-inertial band between 100 hours and 18 hours has also gained some energy compared to the ~~Globcurrent/CMEMS~~ CMEMS MOB-TAC product. However, it is interesting to note that the counter-clockwise spectrum is very similar to ~~Globcurrent/CMEMS~~ CMEMS MOB-TAC, and only slightly above the spectrum of geostrophic current. The second peak at 12h frequency, present in both clockwise and counter-clockwise spectra of the drifter, is not resolved by ~~the reconstructions~~any of the estimates. It corresponds to tidal currents (~~barotopic~~ barotropic near the continental shelves, and mostly baroclinic in open-ocean) not resolved by design ~~in any of the estimates~~of the different products.

The levels of energy do not tell us anything about whether the reconstructions have accurate phases. To examine the accuracy of the phase, we also computed the spectrum of the observations minus the spectrum of the difference between the estimation and the observations. This diagnostic shows how much of the observation variance is explained by the estimation (the thin colored lines). We note that, overall, the levels are similar to the spectra of the estimations suggesting that the phases of the resolved signals are correct. Except for the ~~Globcurrent/CMEMS~~ CMEMS MOB-TAC estimation in the inertial band: the energy is very low (no inertial peak), but the explained variance is much above suggesting that the phases are correct although the energy is damped. This is consistent with what we can observe on Figure 3: the blue curve tends to follow the first oscillation of NIO events, but with a strong attenuation and only immediatly after the wind impulses (by design of the non-convolutive response function).

The resolved variances are also represented in percentages on the bottom-left panel. Not surprisingly, the WOC with its inertial component captures more ~~of the~~ energy in the near-inertial band (30%-40% more), confirming the qualitative results from Figure 3. Also, at lower frequencies, the skill scores are similar between the ~~Globcurrent/CMEMS~~ CMEMS MOB-TAC and WOC, which is consistent. These estimations provide an additional gain of about 10% above the geostrophic current only. However, there is still 40% to 60% current missing in this sub-inertial to inertial frequency range.

Regarding the counter-clockwise scores, the percentages confirm that the ~~Globcurrent/CMEMS~~ CMEMS MOB-TAC and WOC are fairly similar, with slight improvements ~~from~~ compared to geostrophy.

The same diagnostics have been performed in the tropical region between 5°-10°N as shown on Figure 5. In this region the inertial frequency gets shifted toward low-frequencies becoming hard to distinguish from the other dynamics. Nevertheless, the peak is clear (spread between 200 and 50 hours) and the reconstruction skills are comparable to that of the higher latitudes. We note that the WOC spectrum drops more rapidly in the super-inertial band, but where none of the products have significant scores above zero anyway (the phases are not consistent with observations in the super-inertial band~~).~~. This suggests that we

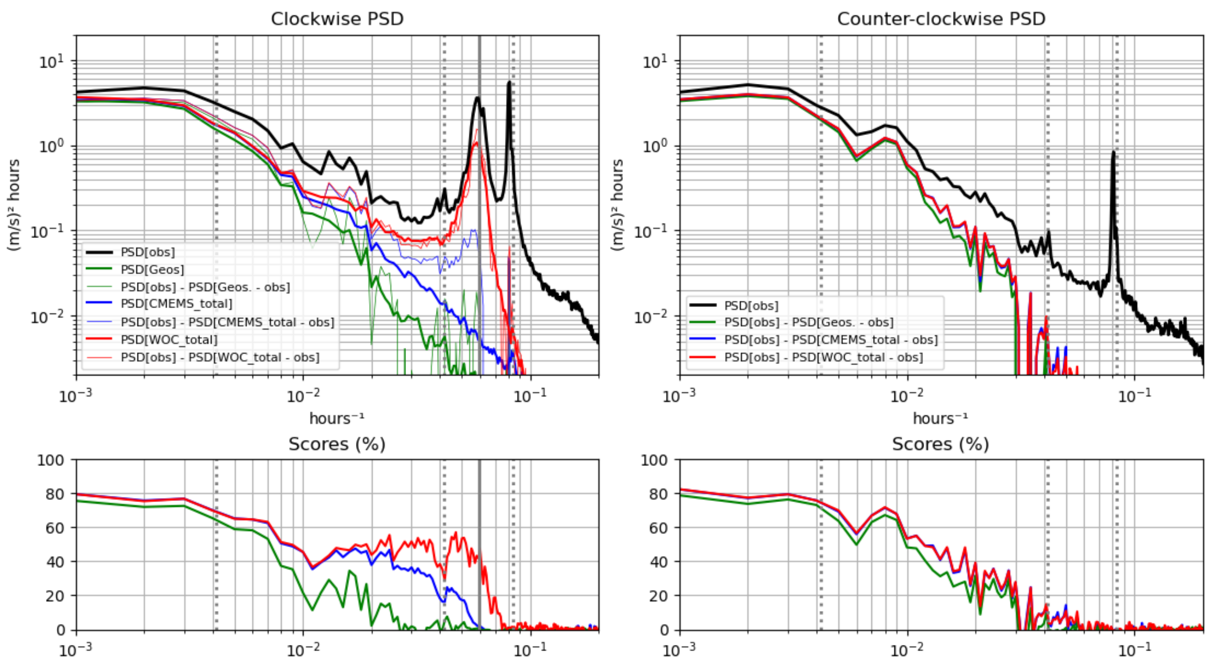


**Figure 4.** Upper-left panel: power spectral density (in the clockwise time-frequency domain between 1000 hours and 2 hours) of the drogued-drifter current observations in the 40°N to 50°N latitude range, in black. The thick-colored curves represent the power spectral densities of the various estimates (~~geostrophic, GlobCurrent/CMEMS~~ geostrophy, CMEMS MOB-TAC and WOC impulse function estimates in green, blue, and red, respectively). The thin-colored curves represent the spectrum of the observations minus the spectra of the difference between the estimation and the observations. Upper-right panel : same, in the counter-clockwise direction. Lower panels : ratio between the thin-colored curves and the black curve of the upper panesl, multiplied by 100, representing the percentages of reconstruction (explained variance). The vertical dotted lines indicate the 240 hours, 24 hours and 12 hours frequencies, respectively from left to right and the vertical plain line indicates the inertial frequency at 45°N (clockwise only).

are not resolving surface currents at short time wavelength in the Tropics, and possible diurnal or semi-diurnal effects are not captured, as discussed later in the conclusion section.

Regarding the counter-clockwise scores, the results are also similar to that of mid-latitudes (with overall less contribution from Altimetry as expected in the tropics).

A graphic of the explained variances as a function of latitude is ~~shown~~ proposed in Figure 6. In this diagnostic, all frequencies are considered, but the view along the latitude dimension, separately for the zonal and meridional current, is instructive. First, we note the strong zonal current variability of the Equatorial currents seen by the drifters. Here, the altimetry contribution owes to the Lagerloef et al. (1999) derivation implemented in the CMEMS geostrophic current product near the Equator, explaining about 1/3 of the variability. This derivation does not provide accurate currents in the meridional direction for which the altimetry contribution is zero near the Equator (right panel). The ~~Globcurrent/CMEMS~~ CMEMS MOB-TAC and WOC estimation provide improvements, more pronounced on the zonal component. At higher latitudes, the zonal and meridional

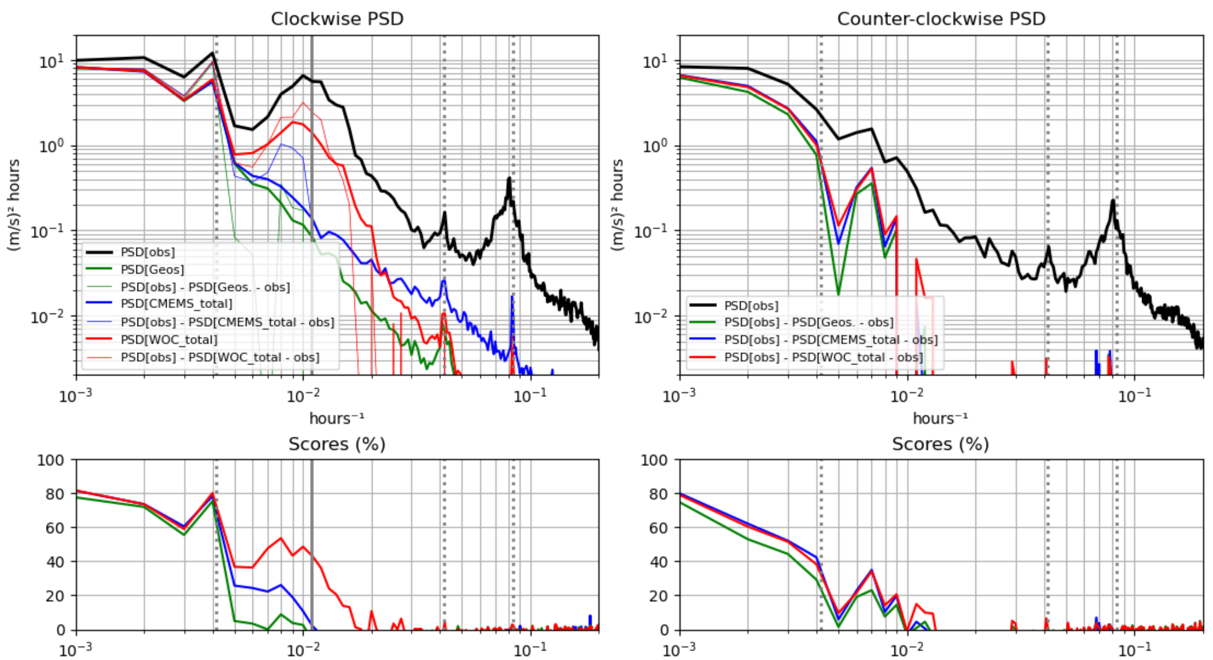


**Figure 5.** Same as Figure 4, averaged between 5°N and 10°N ~~.~~with vertical plain line indicating the inertial frequency at 7.5°N

components show similar explained variances for the different estimations. Overall, if we look at the globally-averaged values from Figure 7, geostrophy explains  40% of the surface current variability, and the WOC estimation brings an additional 12% to 14% for the zonal and meridional components respectively. This is significantly above the ~~Globcurrent/CMEMS~~ CMEMS MOB-TAC that brings 6% to 9% for the zonal and meridional components respectively. This may appear small, but the inertial currents are intermittent and therefore the contribution is certainly much higher at times, particularly ~~just after~~ following a wind event that triggers inertial oscillations. Nevertheless, there is still a large part of unexplained surface current in the drifters (gray areas on the Figure) leaving some room for further scientific investigations that will be discussed in conclusions.

## 5 Characteristics of the response function

~~The response function defined as a bivariate (in the complex 2D plane) convolution over a few days revealed to be~~ If the WOC method revealed efficient in capturing ~~an additional part of the observed surface current~~ some wind-driven current empirically, in particular in the inertial band ~~. It~~ (but not only), it is now interesting to analyze the features of the ~~empirically determined~~ response function, and in particular its potential variations with the season and the latitude.

Figure 8 represents the response function in blue as a function of time, defined between -1 day and +8 days at different latitudes and seasons~~, and separately for the 15 m drogue drifters (blue) and the 0 m undrogue drifters (red)~~. For the purpose of this

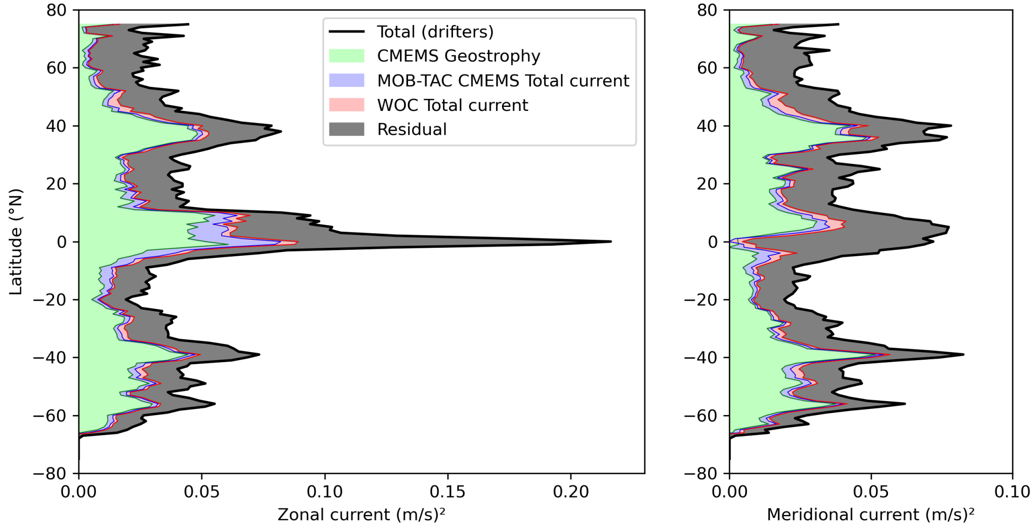


**Figure 6.** Variance of the surface current (zonal component on the left, meridional on the right) as a function of latitude averaged globaly for the drifter database between 2017 and 2020. The black line is for the total current derived from the drifters. The green, blue and red lines are the variance reduction after applying the Geostrophy from CMEMS, the ~~Globcurrent/CMEMS (geostrophy+Ekman) the WOC estimates (geostrophy+Unsteady_Ekman)~~ CMEMS MOB-TAC total current and the WOC total current.

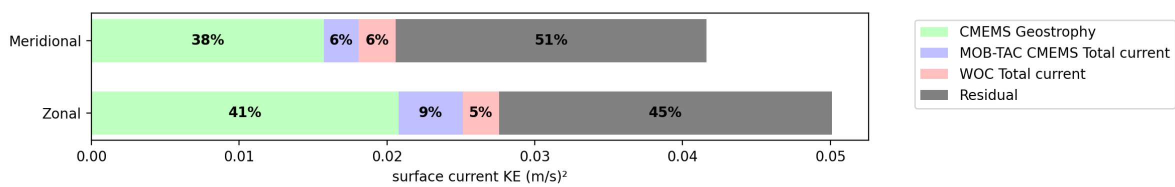


**Figure 7.** Same as Figure 6 averaged globally

diagnostic, we also computed the response function of the undrogued drifters (in red) which gives an interesting comparison, although they are not used for the rest of the study to generate the WOC surface current product.

First, the values of $G$ are close to zero for negative $t'$, suggesting that the future wind stress is not (significantly) related to the present current, which is consistent with the fact that ocean currents respond to the wind forcing, rather than the ocean currents forcing the wind. (We tested a centered window between -8 days and +8 days and also obtained values of $G$ close to zero for negative $t'$.) However, ocean feedbacks to the atmosphere obviously exist (e.g., Renault et al., 2016), but this is not detected in the linear framework of the response function. Then, for positive $t'$, the clear oscillations of $G$ indicate the impact of the wind history over a few days. These oscillations are close to the inertial frequency (varying with latitude: 14.6 hours at

55°N and nearly 3 days at 10°N) as expected by Eq. 10, with an observed decay. Through the convolution, these oscillations act in triggering the inertial oscillation in response to an atmospheric forcing that contains some energy at the Coriolis frequency.

The black curve represents fit for the slab layer response function of Eq. 10. Beyond 12h lag, the slab model, the 15m-drogued-drifter response function, and the undrogued-drifter response functions all show similar behavior. The effect of the seasons at high latitudes is very clear. At 55°N in the winter, the ~~inertia~~ response is twice that of the summer (the thickness of equivalent slab is ~~doubled~~devided by two). In the tropics, the seasonality is much less pronounced as expected. We note that the decay rate is quite similar between winter and summer, and is slightly longer at high latitudes than in the tropics. The decay is likely the combination of two effects at least. One is the actual attenuation of the NIOs in response to a wind impulse, and the second is an additional apparent attenuation due to local modifications of the inertia frequency in response to relative vorticity ~~for instance~~ (e.g. Elipot et al. (2010)), or other factors impacting the phase. Since the response function relies on a least-squares fit, these uncertainties tend to attenuate the actual response, especially at large negative time values.

Beyond the similarities with the slab response, what is particularly interesting are the clear differences in the first few hours of the response function, for both the drogued and undrogued drifters in a different manner. The values at short time lags can be interpreted as the result of dynamics occurring right after the wind impulses (typically after the crossing of an atmospheric front). In the following, we speculate on possible interpretations for the observed differences. A first striking feature is the peak of the real part of the function at zero time-lag for the undrogued drifters. This indicates a direct velocity triggered instantaneously in the wind direction (as the imaginary part remains close to zero). Several effects may explain this peak. A first one is wind-slippage ~~to which undrogued drifters are known to be affected~~ that affects primarily undrogued drifters (e.g. Rio et al. (2014), Laurindo et al. (2017)). The response is indeed immediate to the wind forcing and along its direction, but is not the result of an actual Ocean current. A second one is the Stokes drift from the wind-waves that should also respond rapidly (although not instantaneously) in the wind direction. However, we do not have a clear explanation why the peak seems less pronounced at low-latitudes.

The 15m depth drogued drifters have also interesting departures from the slab in the first few hours. In particular during the winter at high-latitudes. One hypothesis is the presence of temporary re-stratified layers over the very deep mixed layer. This temporary layer would respond to the wind front as a thinner layer in the first hours until the strong mixing (due to the increased wind) transforms the deep mixed layer depth as an active mixing layer, therefore behaving like a slab. In the tropics, we seem to observe an opposite effect at 15m depth with the blue curve reduced in the first 12 hours. This actually might be the result of the same process, but for thinner temporary layers, therefore above the 15m drogue, then destroyed after strong wind impulses.

Although the causes are speculative, this suggests that specific dynamical regimes, fairly different from the slab, are also involved and play a role on the surface current response to wind stress.

Another representation of the same response functions is proposed on Figure 9 along the real and imaginary axes corresponding to the U and V directions respectively. Here, we convolve the response function with a step-function for the wind. This step function, represented by the green arrow along the imaginary axis, is zero for negative time and unitary for positive time. The results, here called the ~~equivalent step-response functions~~ unitary-step response function as represented on the figure, highlight

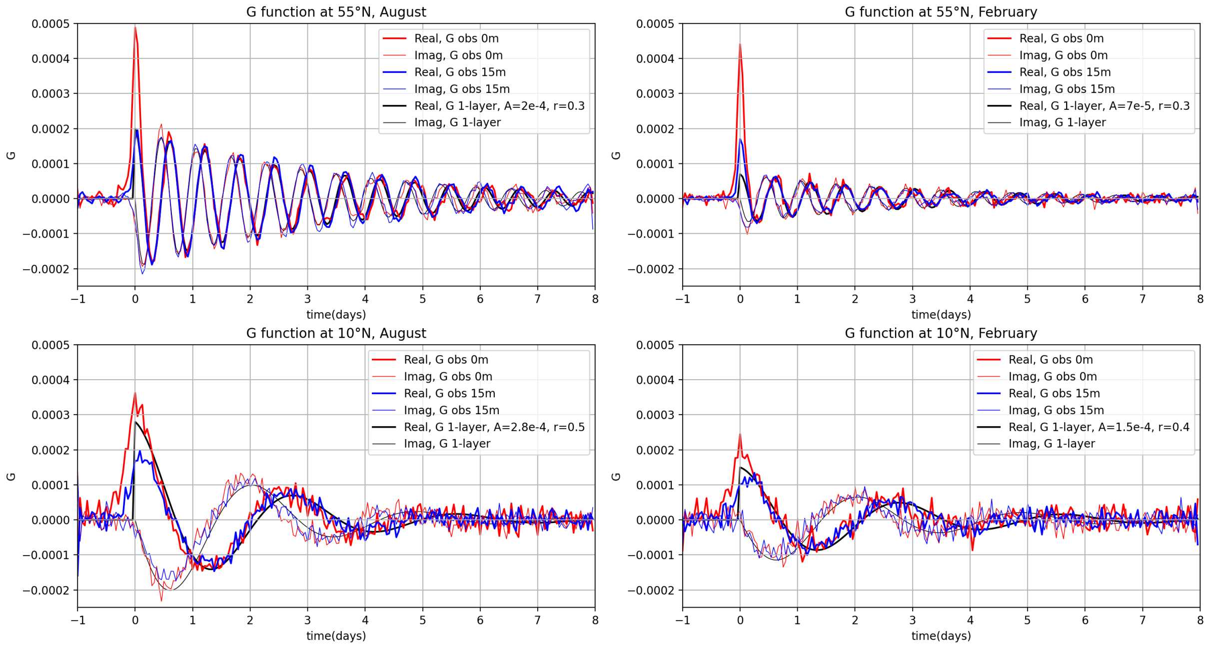


**Figure 8.** ~~Upper-left panel : mean G function in August~~ Upper panel : G function from the first set of parameters in summer at latitude 50°N and longitude -40°E, represented as a function of the $t'$ interval, for the real (plain line) and imaginary parts (dotted line). ~~Upper-right panel : same function in February. Lower panels : same as upper panels, averaged at 10°N~~Lower-left panel : G function from the final parameters with the Fourier time-decomposition truncated at twice the Coriolis frequency. Lower-right panel : same function represented in the Real/Imaginary plane.

additional features. In particular, the low-frequency response ~~, ending at a given angle to the~~ can be directly assessed as being the response to the step function toward infinite time. It corresponds to the point where the curves converge on the figure. This point is to the right of the wind (here in the northern hemisphere) ~~can be clearly assessed both the surface and drogued~~ but at a different angle for the drogued and undrogued drifters. The slab-derived step-response functions have constrained angles in the 70°-80° range for the typical values of damping, which is ~~more~~ higher than what is fitted for the undrogued and drogued drifters. (As is well known, the form of the damping used in the slab model causes the Ekman transport to be slightly less than 90° to the right of the wind.) This again illustrates well the differences and the interest of considering these response function beyond a pure slab dynamic.

## 6 Conclusions and perspectives

This study demonstrated that a purely empirical relation between wind forcing and ~~the~~ some wind-driven surface current ~~(Ekman and inertial currents)~~ can be easily learned from the drifters to provide surface current estimates based on ~~ERA5 wind stress~~ wind stress reanalyses. It provides a potential step forward to the operational ~~Globcurrent MOB-TAC CMEMS surface~~

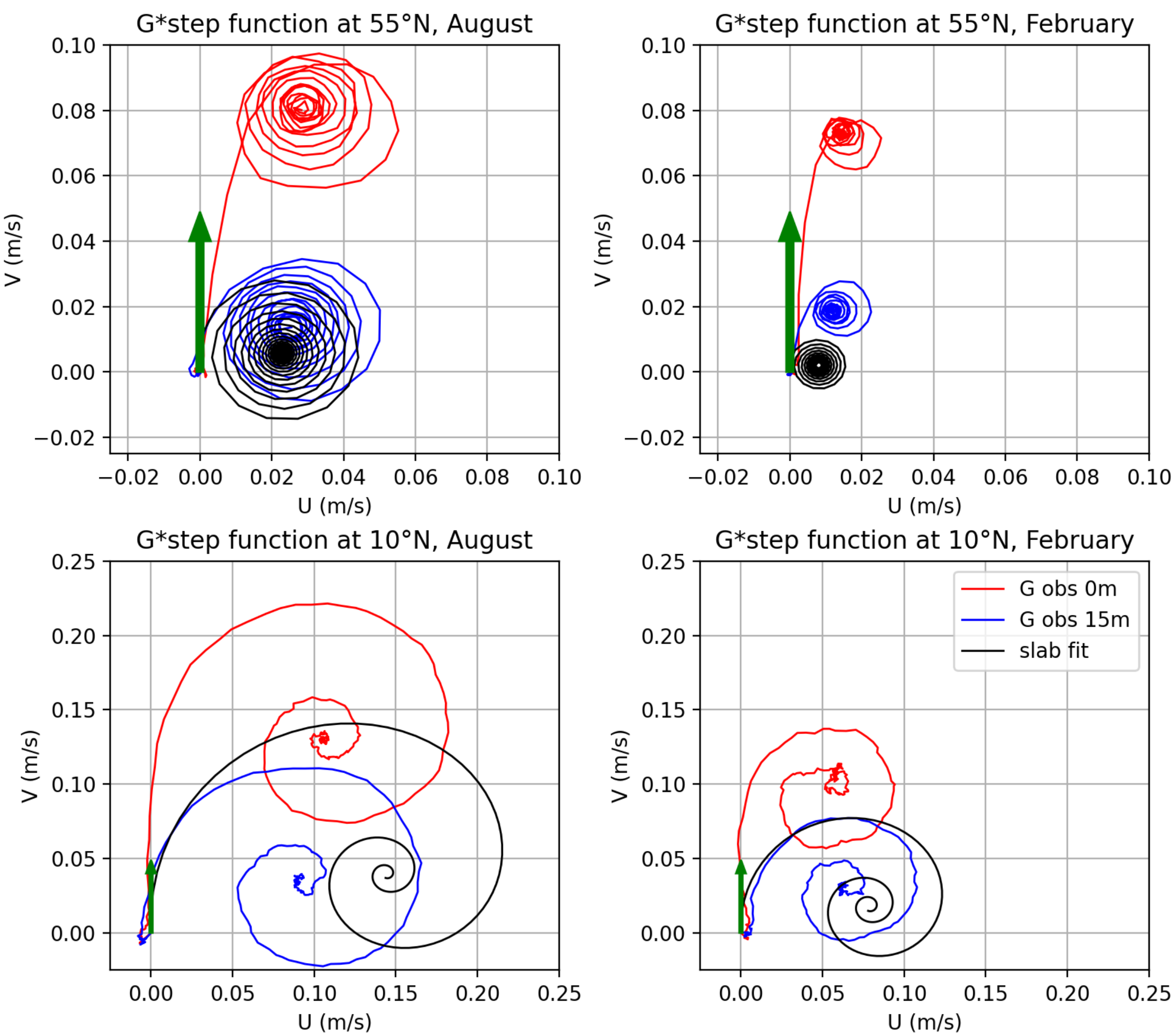


**Figure 9.** Integration of the response function with a unitary-step function of the wind represented by the green arrows. The result, called step-response functions, are represented in the (Real,Imaginary) plane by the red, blue and black lines for the undrogued drifters, drogued drifters and slab respectively.

~~current , based on the same datasets~~ total surface current from the CMEMS MOB-TAC based on a similar methodology and input data but here exploiting higher frequencies through the estimation of an impulse response function. ~~This is now possible globally because of the~~ The recent accumulation of high-quality drifter data at high-frequency ~~. The~~ allowed this step forward. The resulting WOC surface current estimates have been successfully validated with independent observations (drifter data not used in the fit of the impulse function) in comparison with the total surface current from CMEMS MOB-TAC. Although the relative gain of explained variance ~~remains overall of~~ is about 10%~~compared with MOB-TAC CMEMS~~, the gain during intermittent near inertial oscillation events is certainly much higher.

The analysis of the response function learned from the drifters may also yield new insights into the physics. Indeed, we found that the similarities with a slab model response are not always true especially in the first few hours of the response. Speculative causes have been discussed, in relation with the existence of temporary layers. The single damping parameter r of the slab layer model is probably unable to capture all the processes leading to energy dissipation and propagation. The longer term (>12h) response is nonetheless similar with a slab response, for both undrogued and 15m-drogued drifters, and with amplitudes clearly related with the seasons out of the tropics (the thickness of the slab being larger in the winter season). This computation of the response function opens the door for considering further dependencies beyond the seasons and location to better understand the physical processes in the first layers in response to the wind. ~~For instance, additional~~ Additional parameters such as the subsurface density profile or sea state may be introduced as parameters in the empirical computation of the response function. For instance, diurnal and semi-diurnal processes are known to affect the upper Ocean response (Masich et al. (2021), Cherian et al. (2021), Reeves Eyre et al. (2024)) The reduced space imposed to the impulse function do not allow such variation in the response.

These more complex dependencies probably partly explain why a large part of the signal is still unresolved when compared to independent observations. We expect that a lot of progress can be made by considering additional datasets that contain additional information on local sub-surface properties, which could also allow new insights into the physics of the subsurface processes. ~~(Inadequacies of the high-frequency winds~~ The wind stress itself may also feature processes not resolved by the wind-stress reanalysis which may also explain another part the remaining signal, as supported by Klenz et al. (2022). ~~)~~ We could potentially learn a great deal more about the physical processes in upper ocean from global, coincident measurements of ocean vector winds and ocean surface currents that could be measured from satellites (e.g., Rodríguez et al., 2019) by using a data-driven approach to examine the relationship between the two quantities.

*Data availability.* The dataset of surface current generated in this study is available on the World Ocean Circulation ESA project website: https://www.worldoceancirculation.org/

*Competing interests.* The authors declare that no competing interests are present.

*Acknowledgements.* This research was funded by the European Space Agency through the World Ocean Current project (ESA Contract No. 4000130730/20/I-NB ) with complement from the Centre National d'Etudes Spatiales (CNES Contract No. 230376-00 ODYSEA Phase A support) . JTF was supported by the US National Aeronautics and Space Administration (Contract 80GSFC24CA067), via a subaward from the University of California San Diego to the Woods Hole Oceanographic Institution.

## References

Alford, M. H.: Revisiting Near-Inertial Wind Work: Slab Models, Relative Stress, and Mixed Layer Deepening, Journal of Physical Oceanography, 50, 3141–3156, 2020.

Ballarotta, M., Ubelmann, C., Pujol, M.-I., Taburet, G., Fournier, F., Legeais, J.-F., Faugere, Y., Delepoulle, A., Chelton, D., Dibarboure, G., and Picot, N.: On the resolutions of ocean altimetry maps, Ocean Science Discussions, 2019, 1–27, https://doi.org/10.5194/os-2018-156, 2019.

Bendat, J. S. and Piersol, A. G.: Random Data: Analysis and Measurement Procedures (Fourth Edition), Wiley-Interscience, New York, 2010.

Chapron, B., Collard, F., and Ardhuin, F.: Direct measurements of ocean surface velocity from space: Interpretation and validation, Journal of Geophysical Research: Oceans, 110, 2005.

Cherian, D. A., Whitt, D. B., Holmes, R. M., Lien, R.-C., Bachman, S. D., and Large, W. G.: Off-Equatorial Deep-Cycle Turbulence Forced by Tropical Instability Waves in the Equatorial Pacific, Journal of Physical Oceanography, 51, 1575 – 1593, https://doi.org/10.1175/JPO-D-20-0229.1, 2021.

CMEMS-MOB-TAC: 1992-Jan-01 to Present, https://doi.org/10.48670/mds-00327.

Cunningham, H. J., Higgins, C., and van den Bremer, T. S.: The Role of the Unsteady Surface Wave-Driven Ekman–Stokes Flow in the Accumulation of Floating Marine Litter, Journal of Geophysical Research: Oceans, 127, e2021JC018 106, https://doi.org/https://doi.org/10.1029/2021JC018106, e2021JC018106 2021JC018106, 2022.

D'Asaro, E. A.: The energy flux from the wind to near-inertial motions in the surface mixed layer, Journal of Physical Oceanography, 15, 1043–1059, 1985.

Elipot, S. and Gille, S. T.: Ekman layers in the Southern Ocean: spectral models and observations, vertical viscosity and boundary layer depth, Ocean Science, 5, 115–139, https://doi.org/10.5194/os-5-115-2009, 2009.

Elipot, S., Lumpkin, R., and Prieto, G.: Modification of inertial oscillations by the mesoscale eddy field, Journal of Geophysical Research: Oceans, 115, https://doi.org/10.1029/2009JC005679, 2010.

Elipot, S., Lumpkin, R., Perez, R. C., Lilly, J. M., Early, J. J., and Sykulski, A. M.: A global surface drifter data set at hourly resolution, Journal of Geophysical Research: Oceans, 121, 2937–2966, https://doi.org/10.1002/2016JC011716, 2016.

ERA5: https://doi.org/10.24381/cds.adbb2d47.

Flexas, M. M., Thompson, A. F., Torres, H. S., Klein, P., Farrar, J. T., Zhang, H., and Menemenlis, D.: Global Estimates of the Energy Transfer From the Wind to the Ocean, With Emphasis on Near-Inertial Oscillations, Journal of Geophysical Research: Oceans, 124, 5723–5746, https://doi.org/https://doi.org/10.1029/2018JC014453, 2019.

Gill, A. E.: Atmosphere - Ocean Dynamics, Academic Press, San Diego, California, 1982.

Global-Drifter-Program: https://doi.org/10.25921/x46c-3620.

Guinehut, S., B. B. N. T. C. F. C. D. C. e. a.: THE MULTI OBSERVATIONS THEMATIC ASSEMBLY CENTRE OF THE COPERNICUS MARINE ENVIRONMENT MONITORING SERVICE, 9th EuroGOOS International conference, Shom; Ifremer; EuroGOOS AISBL, https://hal.science/hal-03335202v2, 2021.

Hersbach, H., Bell, B., Berrisford, P., Hirahara, S., Horányi, A., Muñoz-Sabater, J., Nicolas, J., Peubey, C., Radu, R., Schepers, D., Simmons, A., Soci, C., Abdalla, S., Abellan, X., Balsamo, G., Bechtold, P., Biavati, G., Bidlot, J., Bonavita, M., De Chiara, G., Dahlgren, P., Dee, D., Diamantakis, M., Dragani, R., Flemming, J., Forbes, R., Fuentes, M., Geer, A., Haimberger, L., Healy, S., Hogan, R. J., Hólm, E., Janisková, M., Keeley, S., Laloyaux, P., Lopez, P., Lupu, C., Radnoti, G., de Rosnay, P., Rozum, I., Vamborg, F., Villaume, S., and Thépaut, J.-N.: The ERA5 global reanalysis, Quarterly Journal of the Royal Meteorological Society, 146, 1999–2049, https://doi.org/https://doi.org/10.1002/qj.3803, 2020.

Higgins, C., Vanneste, J., and van den Bremer, T. S.: Unsteady Ekman-Stokes Dynamics: Implications for Surface Wave-Induced Drift of Floating Marine Litter, Geophysical Research Letters, 47, e2020GL089 189, https://doi.org/https://doi.org/10.1029/2020GL089189, e2020GL089189 10.1029/2020GL089189, 2020.

Klenz, T., Simmons, H. L., Centurioni, L., Lilly, J. M., Early, J. J., and Hormann, V.: Estimates of Near-Inertial Wind Power Input Using Novel In Situ Wind Measurements from Minimet Surface Drifters in the Iceland Basin, Journal of Physical Oceanography, 52, 2417–2430, https://doi.org/10.1175/JPO-D-21-0283.1, 2022.

Lagerloef, G. S. E., Mitchum, G. T., Lukas, R. B., and Niiler, P. P.: Tropical Pacific near-surface currents estimated from altimeter, wind, and drifter data, , 104, 23,313–23,326, https://doi.org/10.1029/1999JC900197, 1999.

Laurindo, L. C., Mariano, A. J., and Lumpkin, R.: An improved near-surface velocity climatology for the global ocean from drifter observations, Deep Sea Research Part I: Oceanographic Research Papers, 124, 73–92, https://doi.org/https://doi.org/10.1016/j.dsr.2017.04.009, 2017.

Lilly, J. M. and Elipot, S.: A Unifying Perspective on Transfer Function Solutions to the Unsteady Ekman Problem, Fluids, 6, https://doi.org/10.3390/fluids6020085, 2021.

Masich, J., Kessler, W. S., Cronin, M. F., and Grissom, K. R.: Diurnal Cycles of Near-Surface Currents Across the Tropical Pacific, Journal of Geophysical Research: Oceans, 126, e2020JC016 982, https://doi.org/https://doi.org/10.1029/2020JC016982, e2020JC016982 2020JC016982, 2021.

OSCAR: 1992-Jan-01 to Present, https://doi.org/10.5067/OSCAR-03D01.

Plueddemann, A. J. and Farrar, J. T.: Observations and models of the energy flux from the wind to mixed-layer inertial currents, Deep Sea Res. II, 53, 5–30, 2006.

Reeves Eyre, J. E. J., Zhu, J., Kumar, A., and Wang, W.: Diurnal Variability of the Upper Ocean Simulated by a Climate Model, Geophysical Research Letters, 51, e2023GL104 194, https://doi.org/https://doi.org/10.1029/2023GL104194, e2023GL104194 2023GL104194, 2024.

Renault, L., Molemaker, M., McWilliams, J., Shchepetkin, A., Lemarié, F., Chelton, D., Illig, S., and Hall, A.: Modulation of Wind Work by Oceanic Current Interaction with the Atmosphere, Journal of Physical Oceanography, 46, 1685 – 1704, https://doi.org/10.1175/JPO-D-15-0232.1, 2016.

Rio, M.-H., Mulet, S., and Picot, N.: Beyond GOCE for the ocean circulation estimate: Synergetic use of altimetry, gravimetry, and in situ data provides new insight into geostrophic and Ekman currents, Geophysical Research Letters, 41, 8918–8925, https://doi.org/10.1002/2014GL061773, 2014.

Rodríguez, E., Bourassa, M., Chelton, D., Farrar, J. T., Long, D., Perkovic-Martin, D., and Samelson, R.: The Winds and Currents Mission Concept, Frontiers in Marine Science, 6, 438, https://doi.org/10.3389/fmars.2019.00438, 2019.

Shrira, V. I. and Almelah, R. B.: Upper-ocean Ekman current dynamics: a new perspective, Journal of Fluid Mechanics, 887, A24, https://doi.org/10.1017/jfm.2019.1059, 2020.

Taburet, G., Sanchez-Roman, A., Ballarotta, M., Pujol, M.-I., Legeais, J.-F., Fournier, F., Faugere, Y., and Dibarboure, G.: DUACS DT2018: 25 years of reprocessed sea level altimetry products, Ocean Science, 15, 1207–1224, https://doi.org/10.5194/os-15-1207-2019, 2019.

WOC: https://data-cersat.ifremer.fr/projects/woc/products/theme3/ocean_currents/woc-l4-cureul-natl-1h/v2.0/.

Young, W. and Jelloul, M. B.: Propagation of near-inertial oscillations through a geostrophic flow, Journal of marine research, 55, 735–766, 1997.

Yu, X., Ponte, A. L., Elipot, S., Menemenlis, D., Zaron, E. D., and Abernathey, R.: Surface Kinetic Energy Distributions in the Global Oceans From a High-Resolution Numerical Model and Surface Drifter Observations, Geophysical Research Letters, 46, 9757–9766, https://doi.org/https://doi.org/10.1029/2019GL083074, 2019.